remote sensing

MDPI

Article

Fire Monitoring Algorithm and Its Application on the Geo-Kompsat-2A Geostationary Meteorological Satellite

Jie Chen [1,2], Wei Zheng [1,2], Shuang Wu [3,*], Cheng Liu [1,2] and Hua Yan [1,2]

[1] Key Laboratory of Radiometric Calibration and Validation for Environmental Satellites, National Satellite Meteorological Center (National Center for Space Weather), China Meteorological Administration, Beijing 100081, China; chenjie@cma.gov.cn (J.C.); zhengw@cma.gov.cn (W.Z.); liucheng@cma.gov.cn (C.L.); yanhua@cma.gov.cn (H.Y.)
[2] Innovation Center for FengYun Meteorological Satellite (FYSIC), Beijing 100081, China
[3] Heilongjiang Eco-Meteorology Center, Harbin 150030, China
* Correspondence: wushuanghlj@163.com

Abstract: Geo-Kompsat-2A (GK-2A) is the third new-generation geostationary meteorological satellite that orbits Asia and monitors China and its surrounding areas, following the Himawari-8 and Fengyun-4A satellites. The nadir point positioning and satellite channel parameters of the GK-2A are better than those of the Himawari-8 and FY-4A, which are more conducive to fire monitoring in China. In this study, a new fire detection algorithm is proposed based on GK-2A satellite data. That is, considering the large solar zenith angle correction for reflectance and the proportion information of background pixels in the existing spatial threshold method, fires under the different underlying surface types and solar radiation states can be automatically identified. Moreover, the accuracy of the Himawari-8 fire monitoring algorithm and the present algorithm of GK-2A is compared and analyzed through the ground truth fire spot data. The results show that compared with the original fire monitoring algorithm with fixed parameter thresholds, the brightness temperature difference of this algorithm is reduced by 0.55 K, and the correction coefficient is reduced by 0.6 times, the fire can be found earlier, and the monitoring sensitivity is improved. According to the practical fire case, the present fire monitoring algorithm of GK-2A has better monitoring accuracy than the fire monitoring algorithm of Himawari-8. The present fire monitoring algorithm of GK-2A can meet the fire monitoring requirements under different sun angles, different cloud cover ratios and vegetation ratios with good versatility.

Keywords: Geo-Kompsat-2A satellite; geostationary meteorological satellite; forest fire detection

Citation: Chen, J.; Zheng, W.; Wu, S.; Liu, C.; Yan, H. Fire Monitoring Algorithm and Its Application on the Geo-Kompsat-2A Geostationary Meteorological Satellite. *Remote Sens.* **2022**, *14*, 2655. https://doi.org/10.3390/rs14112655

Academic Editor: John J. Qu

Received: 30 March 2022
Accepted: 28 May 2022
Published: 1 June 2022

1. Introduction

As one of the major natural disasters, forest and grassland fires can seriously damage the ecological environment, endangering people's life and property [1–4]. Thus, timely and accurate fire information is of great significance for fire monitoring and early warning. With the development of remote sensing technology, the application skill of polar-orbiting meteorological satellites in forest and grassland fire detection has been well developed [5–8]. In China, Fengyun series satellites have been used to monitor forest and grassland fires in the Greater Hinggan Mountains, Inner Mongolia, Sichuan Province and other places for more than 30 years [9–11]. Numerous cases have shown that algorithms are also used in the Moderate Resolution Imaging Spectro-radiometer, National Oceanic and Atmospheric Administration series and other satellites to monitor fires [12–16]. However, due to the observation frequency of polar-orbiting meteorological satellites and their observation periods, they have difficulty in capturing rapidly changing forest and grassland fires in time and continuously and dynamically monitoring the same fire.

In recent years, many satellites for forest and grassland fire detection have been launched, such as the Himawari-8 launched by Japan [17,18], GOES-R/S/T by the United

States and Geo-Kompsat-2A (GK-2A) by South Korea. Compared with the previous satellites, these new-generation geostationary meteorological satellites have been improved in spatial resolution and observation frequency. Thus, they have become an essential means of forest and grassland fire monitoring and early warning. At present, the main fire monitoring algorithms used for polar orbit satellites and geostationary satellites are contextual. Many reports that worked on the improvement of the MODIS fire monitoring algorithm that had been published since the original MODIS fire monitoring algorithm released by Kaufman and Justice in 1998 [19,20]. However, most studies were focused on the brightness temperature threshold of satellite fire point identification and the refined calculation of background pixel brightness temperature. The fixed threshold method was used in most algorithms, which might lead to misjudgment when it was used in different seasons and climate regions. In addition, the impact of the change of solar angle on the accuracy of the algorithm was not considered in most studies. With the application of geostationary meteorological satellites in fire monitoring, some approaches had been performed to solve the above problems. Based on the observation characteristics of the Himawari-8 geostationary satellite, Chen et al. used multivariable thresholds to explore the application of Himawari-8 satellite data in regional fire monitoring in China. Studies have shown that the it can obtain fire information earlier and has a strong advantage in fire detection.

The AHI (Advanced Himawari Imager) sensor on Himawari-8 provides high-frequency satellite data at 10-min intervals. It is suitable for real-time fire monitoring over a large spatial and temporal scale [21]. Wickramasinghe et al. developed an algorithm based on data of the Himawari-8 for Western Australia and compared it with MODIS fire monitoring data in the same area. The results show that the daily AHI-FSA omission error was only 7%. High temporal frequency data also results in AHI-FSA observing fires, at times, three hours before the MODIS overpass with much-enhanced detail on fire movement [22]. The influence of the sun angle on the threshold was not included in the algorithm used for Himawari-8, nor the influence of the underlying surface proportion and cloud coverage on the background brightness temperature. Therefore, the accuracy of fire point identification was reduced under the condition with complex underlying surface and cloud coverage.

The GK-2A has similar observation frequency and spatial resolution to the Himawari-8 satellites [23]. However, the sub-satellite point of the GK-2A is at 128.2°E, which is about 1000 km closer to China than that of the Himawari-8. Therefore, the GK-2A has better sensitivity and accuracy for fire detection in China.

Moreover, as a new generation of geostationary meteorological satellites, the GK-2A, has a similar band range to that of the Himawari-8, which covers the visible light band to the far-infrared band. Therefore, the fire spot identification algorithm of the GK-2A is similar to that of the Himawari-8 [24–26].

In this study, an automatic fire identification algorithm with large solar zenith angle correction and fractional vegetation coverage is developed based on the GK-2A satellite data and the spatial threshold method from the Himawari-8 geostationary meteorological satellite.

Based on this algorithm, the "3.30" forest fire in Xichang City, Sichuan Province, in March 2020 is used as an example to introduce the application of the GK-2A in forest fire detection. The research results demonstrate that the GK-2A can continuously monitor fire information such as fire spot position and fire intensity. Furthermore, the dynamic development of forest fires can be tracked by analyzing the fire images and fire detection information continuously observed over multiple times.

2. Date and Method

2.1. Study Area

The geostationary satellite Geo-Kompsat-2A began operating on 4 December 2018. It is positioned above the equator at 128.2°E. The study area is the Geo-Kompsat-2A full-disk data. Since the GK-2A monitors the entire disk area, the ground verification workload is large. Guangdong, Guangxi and other southern provinces with high forest

fire incidence were selected. The accuracy of Himawari-8 fire point monitoring algorithm and GK-2A's new algorithm is compared based on the ground feedback information of the China Southern Power Grid Corporation in April 2021. The fire incident in Xichang, Sichuan Province in 2020 was taken as an example to analyze the fire point monitoring in minutes.

2.2. Instrument Features

Compared with the traditional geostationary meteorological satellites, the advanced meteorological imager (AMI) carried by the GK-2A has relatively higher radiometric, spectral and spatio-temporal resolutions. The GK-2A is a three-axis attitude control satellite with a length of about 9 m and a mass of about 3500 kg at launch. The main parameters of the GK-2A are listed in Table 1. The GK-2A/AMI covers 16 channels, including visible, near-infrared, mid-infrared and far-infrared channels, with spatial resolutions of 0.5 km, 1 km and 2 km. The channel parameters of the GK-2A/AMI are shown in Table 2.

Table 1. Major specifications of the GK-2A.

Index	Specifications
Altitude control	Three-axis stabilization
Size during operation	Launch: 2.9 × 2.4 × 4.6 (m) Orbit: 3.8 × 8.9 × 4.6 (m)
Mass	Launch mass:3.2ton@mission period 3.5ton@max availability
Design lifetime	Meteorological Mission:10 years
Geostationary position	128.2 degrees East
Imager	Advanced Meteorological Imager (AMI)
Space weather monitor	Particle detector (PD) Magnetometer (MG) Charging monitor (CM)
Communication	AMI data transmission AMI data broadcast system Command and telemetry

Table 2. Major parameters of GK-2A/AMI channels.

Bands	Center Wavelength		Band Width (max, μm)	Resolution (km)	Bite Depth
	Min (μm)	Max (μm)			
VIS0.4	0.431	0.479	0.075	1	11
VIS0.5	0.5025	0.5175	0.0625	1	11
VIS0.6	0.625	0.66	0.125	0.5	12
VIS0.8	0.8495	0.8705	0.0875	1	13
NIR1.3	1.373	1.383	0.03	2	12
NIR1.6	1.601	1.619	0.075	2	11
IR3.8	3.74	3.96	0.5	2	14
IR6.3	6.061	6.425	1.038	2	12
IR6.9	6.89	7.01	0.5	2	13
IR7.3	7.258	7.433	0.688	2	13
IR8.7	8.44	8.76	0.5	2	13
IR9.6	9.543	9.717	0.475	2	13

Table 2. *Cont.*

Bands	Center Wavelength		Band Width (max, μm)	Resolution (km)	Bite Depth
	Min (μm)	Max (μm)			
IR10.5	10.25	10.61	0.875	2	13
11.2	11.08	11.32	1.0	2	13
12.3	12.15	12.45	1.25	2	13
13.3	13.21	13.39	0.75	2	13

2.3. Data Preprocessing

2.3.1. Channel Calibration and Reflectivity Correction

The initial data in the 16 GK-2A/AMI channels are used as the digital number. The reflectivity and brightness temperature values on each channel can be obtained through the official calibration lookup table. The calibration function diagram of the AMI channels (Figure 1) indicates that the reflectivity calibrations of channels 1–6 are by linear functions, while the brightness temperature calibrations of channels 7–16 are by nonlinear functions. The bit depth of digital number values is 11 bit on channels 1, 2 and 6, 12 bit on channels 3 and 5, and 13 bit on channel 4. Thus, channel 4 has the largest bit depth, widest range and the most detailed reflection information. Channels 7–16 are infrared channels. Among them, channel 7 has a bit depth of 14 bit, with a maximum brightness temperature of more than 400 K, containing the most abundant brightness temperature information. The value ranges of the brightness temperature on channels 8–16 are closer, between 100 K and 350 K [27,28].

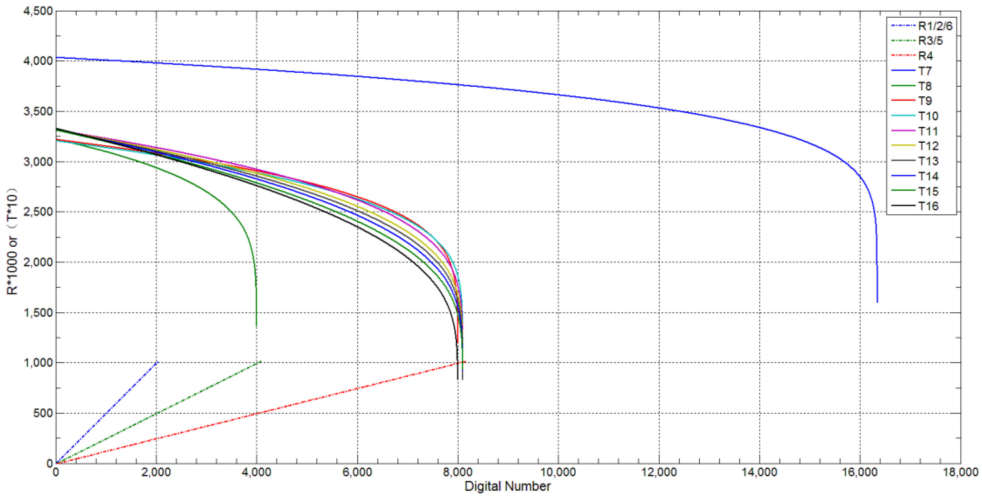

Figure 1. Function diagram of the GK-2A/AMI channel lookup table.

Since the solar zenith angle variation causes the differences in observations, the reflection on each channel needs to be corrected before being used. The traditional solar zenith angle correction method is shown in Equation (1).

$$R' = R/\cos(\theta) \quad (1)$$

where R denotes the original reflectivity from satellite observations, R' the reflectivity corrected by the solar zenith angle, and θ the solar zenith angle. The GK-2A satellite orbit is located at 35,800 km above the equator and remains relatively stationary with the earth, i.e., in a fixed-point observation mode. This observation mode can realize the all-time observation, i.e., there is full coverage of the solar zenith angle. When the solar zenith angle approaches 90°, $\cos(\theta)$ is infinitely close to 0, resulting in an anomalous value of R'.

Therefore, for the large solar zenith angle observation, a correction should be performed by Equation (2).

$$R' = R/\cos(\theta * (1.0 - 1.3 * \sin(0.05 * \theta))) \quad (2)$$

Figure 2 presents the differences between the results of Equations (1) and (2). Obviously, when the solar zenith angle is less than 30°, the correction results from Equations (1) and (2) are relatively consistent. However, the differences of the two correction methods gradually enlarge with the increase of the solar zenith angle, especially the solar zenith angle of more than 60°. Due to the characteristics of fixed-point observation, the GK-2A often works with the solar zenith angle exceeding 60°. Thus, the observation results from the satellite need special treatment. The difference before and after the reflectivity correction by Equation (1) (blue line) is more than 50 times, while the difference from Equation (2) (green line) is reduced to about six times. A similar situation can be found from the ratio curves (red line) of the two methods. Therefore, the reflectivity correction by using Equation (2) is more scientific.

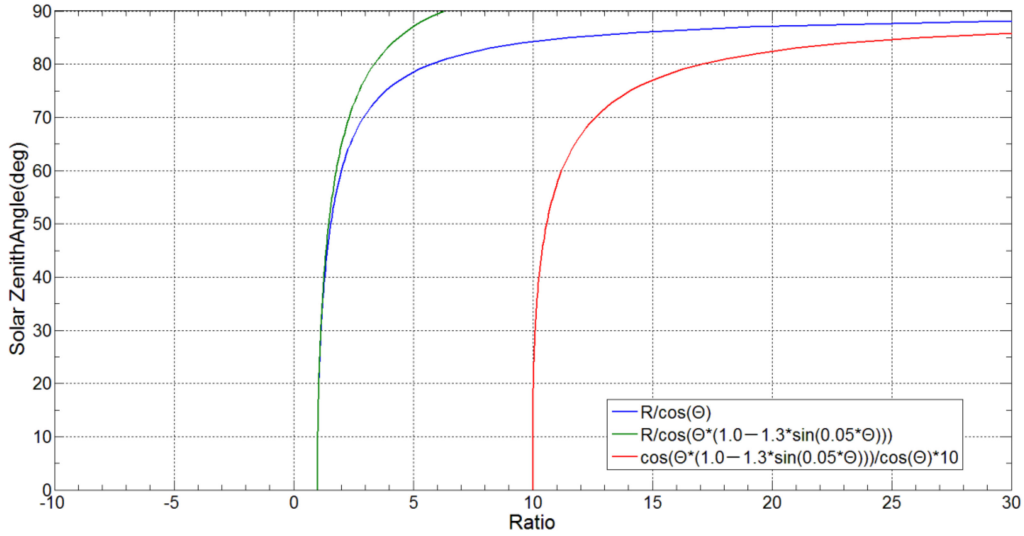

Figure 2. Comparison of different reflectivity correction methods.

2.3.2. Location Correction

The GK-2A adopts the geostationary satellite normalized projection defined by the Low/High Rate Information Transmission issued by the Coordination Group for Meteorological Satellites, and the geographic coordinates are calculated based on the World Geodetic System 84 reference ellipsoid [29]. The positioning errors of fire spots are the largest influencing factor of fire detection by satellite remote sensing, which is influenced by numerous factors, such as the observation mode of sensors, satellite attitude, projection mode and elevation. Among them, elevation is the most common factor causing positioning deviation. The mountainous areas in southern China are far from the sub-satellite point of the GK-2A, with complex terrain and large topographic relief. As satellite positioning accuracy cannot be ignored in fire detection and application, geometric correction is necessary for processing fire spots from satellite remote sensing [30]. Figure 3 shows that topographic relief can cause a displacement in satellite image positioning.

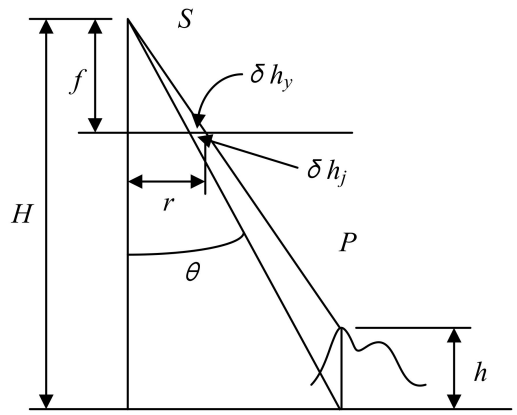

Figure 3. Influence of topographic relief on satellite positioning.

Under the condition of vertical photography, the image point displacement caused by the topographic relief can be expressed as Equation (3).

$$\delta h = \frac{r}{H} h \tag{3}$$

where h indicates the height difference between the ground point corresponding to the image point and the datum plane, H the height of the platform relative to the datum plane, and r the distance from the image point to the bottom point.

The 30 m × 30 m elevation data is used to correct the projection errors caused by topographic changes in high-altitude areas in China. Figure 4 is the elevation correction effect map of high altitudes (Tibetan Plateau, upper part of Figure 4) and low altitudes (Hainan, lower part of Figure 4) projected by the GK-2A. The yellow line is the vector line of the land and water boundary. When the land and water boundary matches the water and land of the GK-2A satellite image, the positioning is accurate. Obviously, the higher the elevation, the greater the correction amplitude. In addition, there is almost no change in the positioning displacement before and after the correction in low altitude areas. High-precision elevation data can be used to assess the impact of elevation on satellite positioning, thereby correcting the positioning.

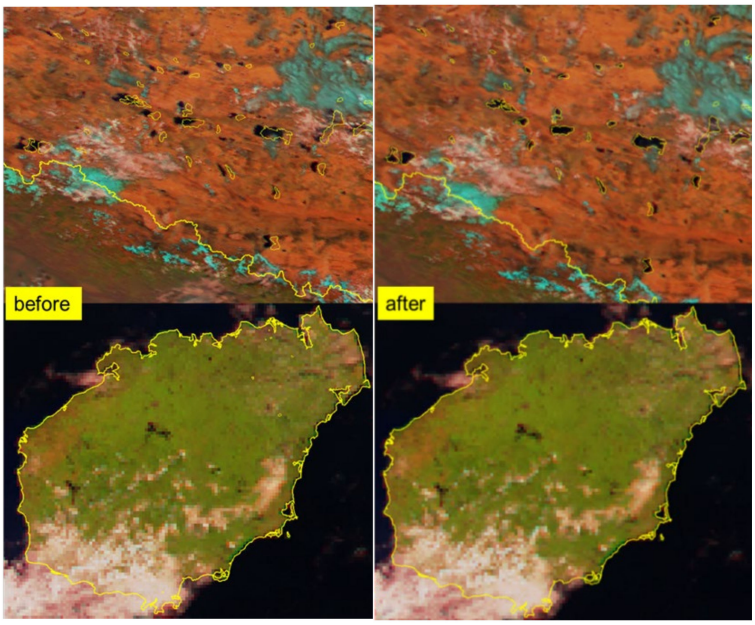

Figure 4. Positioning correction effect of the GK-2A remote sensing images at different elevations.

2.4. Method

2.4.1. Principle

The basic principle of fire spot identification by remote sensing technology relies on two conditions, i.e., the enhancement of thermal radiation caused by increasing temperature and the difference of growth ranges of various thermal infrared channels. According to the Stefan Boltzmann law, the energy increase is proportional to the fourth power of the brightness temperature. The temperature change of a high-temperature heat source is favorable to identify the heat source. Wien's displacement law indicates that the brightness temperature is inversely proportional to the central wavelength of radiation, i.e., the radiation wavelength becomes shorter with the increasing brightness temperature. Suppose the normal temperature of bare ground surface is 300 K, and the peak wavelength of radiation is about 11 μm. When the temperature of biomass combustion reaches more than 1000 K, the peak wavelength of radiation is about 3.5 μm. The channels of GK-2A sensors include 3.9 μm, 11.2 μm and 12.3 μm, which are conducive to fire spot identification.

2.4.2. Algorithm

To realize the automatic fire spot identification by the GK-2A, we improve the fire spot detection algorithm used by the Himawari-8 satellite in this study based on characteristics of the GK-2A sensor channels [16]. Moreover, the solar zenith angle and underlying surface type proportion are taken into consideration in this algorithm. Figure 5 shows the flow chart of the fire spot identification.

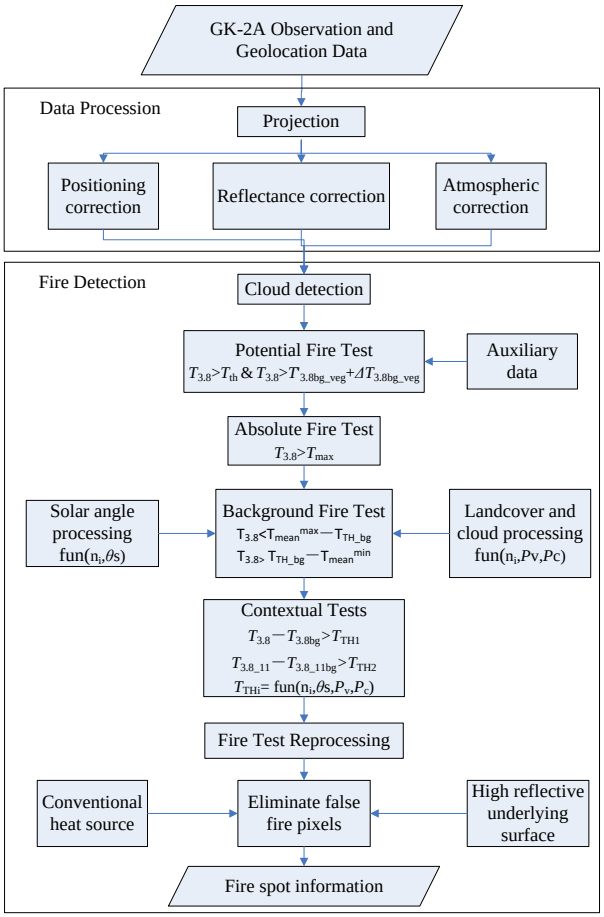

Figure 5. Flow chart of fire identification by the GK-2A satellite.

The main differences of fire the spot identification algorithms between the GK-2A and the Himawari-8 are reflected in the calculation of brightness temperature at background pixels and the dynamic threshold of fire spot pixel identification.

Calculation of Brightness Temperature at Background Pixels

The effective background pixels and their brightness temperature are essential physical quantities for fire spot identification in this study, and appropriate pixels are necessary for calculating brightness temperature at background pixels. If the brightness temperature of the pixel is excessively high, it can raise the background brightness temperature, thus resulting in missing detection. Conversely, low-temperature pixels can reduce the brightness temperature of background pixels, causing false detection. Therefore, pixels with excessively high and low brightness temperature are regarded as invalid pixels. To extract effective pixels, we propose the condition judgment method of underlying surface type differentiation based on previous studies on fire spot operational identification from the Himawari-8 and Fengyun-4A satellite images, i.e., if the brightness temperature at the mid-infrared channel meets Equations (4) and (5), this pixel can be determined as an effective background pixel.

$$T_7 < \overline{T_{mean}^{max}} - T_{TH\_bg} \tag{4}$$

$$T_7 > T_{TH\_bg} - \overline{T_{mean}^{min}} \tag{5}$$

$$T_{TH\_bg} = 2 * \overline{T_7} - \delta T_7 \tag{6}$$

where $\overline{T_{mean}^{max}}$ indicates the average brightness temperature at the mid-infrared channel in the window area that is higher than the brightness of the identified pixel when the land type in the window area is not consistent with that of the identified pixel. $\overline{T_{mean}^{min}}$ is similar to, and the only difference is that is lower than the brightness of the identified pixel. T_{TH_bg} denotes the discrimination threshold of the effective background pixels, $\overline{T_7}$ and δT_7 are the average value and standard deviation of brightness temperature at all mid-infrared channels in the window area.

Based on the obtained effective background pixels, the average brightness value of the effective background pixels in the region to be judged can be calculated, i.e., the background brightness temperature is obtained. 3×3 pixels are selected in the initial window area. If the number of effective pixels is less than 20% of the total pixels in the window area, the window area will be expanded to continue screening. If the window area has 51×51 pixels (maximum number) and still does not meet the above condition, the pixels to be judged are marked as non-fire pixels.

Confirmation of Fire Spot Pixels

The fire spot pixels can be obtained by using the growth difference of the brightness temperature of the identified pixels and background effective pixels at mid-infrared and far-infrared channels [14,15]. That is, if the brightness temperature satisfies Equations (7) and (8) at the same time, the corresponding pixel can be determined as a fire spot pixel.

$$T_7 - T_{7bg} > T_{TH1} \tag{7}$$

$$T_{7\_14} - T_{7\_14bg} > T_{TH2} \tag{8}$$

where T_7 and T_{7bg} represent the mid-infrared brightness temperature of the identified pixel and the background pixel, T_{7_14} and T_{7_14bg} denote the brightness difference between the mid-infrared and far-infrared channels in the identified pixel and background pixel, and T_{TH1} and T_{TH2} indicate the dynamic thresholds calculated by Equations (9) and (10).

$$T_{TH1} = n_1 \times \delta T_{7bg} \tag{9}$$

$$T_{TH2} = n_2 \times \delta T_{7\_14bg} \tag{10}$$

where δT_{7bg} represents the standard deviation of the brightness temperature of the mid-infrared channel at effective background pixel, δT_{7_14bg} the standard deviation of the brightness temperature difference between the mid-infrared and far-infrared channels at the effective background pixel, n_1 the correction coefficients of T_{TH1}, and n_2 the correction coefficients of T_{TH2}. Note that identification thresholds are obtained based on numerous historical real fire spot samples, which vary with observation time and areas.

Treatment of Solar Zenith Angle and Special Underlying Surface

Geostationary satellites have high-frequency and all-time observation characteristics, and their complex fire spot identification conditions are complex. The mid-infrared channel is at the junction of reflection and radiation. Therefore, if the radiation signal is strong, the reflected signal is easy to be captured in this channel as the radiation information. The reflected signal is affected by the solar zenith angle, clouds and special underlying surfaces. That is, the solar radiation signal is reflected into the satellite sensor at identified pixels, which is easy to be regarded as a thermal radiation signal. Therefore, the radiation results obtained from the satellite images need to be corrected for the effects of solar zenith angle and special underlying surfaces such as clouds.

(1) Treatment of solar altitude angle and fractional vegetation coverage

By using the underlying surface information, we process the correction coefficients of the dynamic thresholds in the improved algorithm. In addition, we analyze the influence law of θ_s (solar altitude angle of the pixel to be judged) and P_V (the proportion of non-vegetation pixels in the window area) on the correction coefficients to obtain n_i^* (the modified coefficient), as shown in Equation (11).

$$n_i^* = \begin{cases} n_i \times (1 + sin(\theta_s)) \times (1 + P_V) & ;\theta_s \leq 45^\circ \\ n_i \times (1 + 1.2sin(\theta_s)) \times (1 + P_V); & \theta_s > 45^\circ \end{cases} \quad (11)$$

where n_i denotes the initial background coefficients, and i = 1 or 2. Under initial conditions, n_1 and n_2 are equal to 3 and 3.5, respectively. Note that n_i increases with θ_s and P_V to reduce the false detection caused by the solar reflection signal.

(2) Treatment of cloud interference effects

As a special underlying surface, clouds usually have the characteristics of low brightness, high reflectivity and special geometric structure. When the identified pixel is at the edges and gaps of clouds, the effective background brightness temperature may be reduced due to the cloud brightness temperature, which makes the brightness of the identified pixel easy to meet the fire point identification conditions. Moreover, the specular reflection effect of solar radiation caused by the unique structure of clouds may result in the false detection of fire spots. Therefore, an adaptive correction method for the proportion of cloud pixels is developed, as shown in Equation (12).

$$\delta T_{ibg}^* = \begin{cases} 2 \times (1 + P_c) & \delta T_{ibg} \leq 2K \\ \delta T_{ibg} \times (1 + P_c) & 2K \leq \delta T_{ibg} \leq 4K \\ 4 \times (1 + P_c) & \delta T_{ibg} \geq 4K \end{cases} \quad (12)$$

where the value of i ranges from 7 to 14. Additionally, δT_{ibg}^* and δT_{ibg} indicate the corrected standard deviation and the original standard deviation at the window area, and P_c denotes the proportion of cloud pixels in the window area. The identification threshold increases with P_c around the identified pixel, i.e., the standard of fire spot identification is raised to effectively reduce the false detection of fire spots at the edge of clouds.

Elimination of False Fire Spots

Perennial high-temperature sources and flare spots, such as factories, photovoltaic power plants and cities, are the main factors of the false fire spot detection and need to

be excluded in the fire spot identification process. Artificial heat sources are the main components of the perennial high-temperature sources, which are excluded by using auxiliary data such as land cover type. Flare spots are filtered out by the flare angle threshold, and the flare angle (θ_r) is obtained according to Equation (13).

$$\theta_r = \arccos(sin\theta_V sin\theta_s cos\psi + cos\theta_V cos\theta_s) \quad (13)$$

where ψ represents the relative azimuth, and θ_V indicates the observation zenith angle. If both the visible reflectance and infrared reflectance are greater than 0.3, and the flare angle is less than 30°, the pixel is regarded as a flare spot.

3. Results and Discussion

3.1. Improved Fire Monitoring Algorithm

Considering the maturity of the algorithm and the proximity of instrument characteristics, this paper investigates the satellite fire monitoring algorithms of MODIS and Himawari-8/AHI, respectively. Giglio described the Collection 6 (C6) MODIS fire detection algorithm which could address limitations of the Collection 5 fire product. It was proved that C6 could reduce the false alarms caused by small forest clearings and the oversight of fires hidden by dense smoke. However, there are still limitations in the study of dynamic threshold [14,31–33]. Na, Li monitored the overall process of grassland fires that occurred on the border area of China and Mongolia using bands 7, 4, and 3 of the Advance Himawari Imager (AHI) data, in conjunction with a threshold algorithm and a visual interpretation method. It was found that the dynamic change of a grassland fire could be tracked and the spread speed and direction could be predicted based on AHI data [34,35].The dynamic monitoring of the whole process of fire development based on himawari-8 satellite data was also realized in our previous report. However, the observation signal of the geostationary meteorological satellite is greatly affected by the change of solar angle, while the influence of solar angle change is not considered in previous studies.The above-mentioned satellite algorithms have insufficient research on the dynamic threshold, and the observation signal of Himawari-8/AHI satellite changes greatly with the change of the sun angle. The GK-2A fire point algorithm is designed to solve the problem of dynamic threshold value monitoring of fire point under the observation of the full solar elevation angle of the geostationary meteorological satellite. The method based on variable threshold function under the conditions of different sun angles, cloud coverage and vegetation coverage improves the misjudgment caused by the sun reflection at the cloud edge and the sparse vegetation underlying the surface, and improves the all-day fire point of the geostationary meteorological satellite. The accuracy of monitoring improves the sensitivity of micro-fire monitoring (Table 3).

Table 3. Fire monitoring algorithm for different satellites.

	MODIS(VIIRS)	Himawari-8	GK-2A
Potential Fire Test	Daytime: $T_4 > 310$ & $\Delta T > 10$ Nighttime: $T_4 > 305$ & $\Delta T > 10$ ($T_4 > T_{min}$ $\Delta T > \Delta T_{min}$)	$T_{3.9} > T_{th}$ $T_{3.9} > T'_{3.9bg\_veg} + \Delta T_{3.9bg\_veg}$	$T_{3.8} > T_{th}$ $T_{3.8} > T'_{3.8bg\_veg} + \Delta T_{3.8bg\_veg}$
Absolute Fire Test	Daytime: $T_4 > 360$ Nighttime: $T_4 > 320$ ($T_4 > T_{abs}$)	$T_{3.9} > T_{max}$	$T_{3.8} > T_{max}$

Table 3. *Cont.*

	MODIS(VIIRS)	Himawari-8	GK-2A
Background Fire Test	Daytime: $T_4 > 325 \& \Delta T > 20$ Nighttime: $T_4 > 310$ & $\Delta T > 10$	$T_{3.9} > T_{3.9bg} + T$	$T_{3.8} < \overline{T_{mean}^{max}} - T_{TH\_bg}$ $T_{3.8} > T_{TH\_bg} - \overline{T_{mean}^{min}}$
Contextual Tests	$\Delta T > \Delta T_b + 3.5 \times \delta \Delta T$ $\Delta T > \Delta T_b + 6k$ $T_4 > T_{4b} + 3 \times \delta 4$ $T_{11} > T_{11b} + \delta_{11} - 4k$ $\delta'_4 > 5$ k	$T_{3.9} > T_{3.9bg} + n_1 \times \delta T_{3.9bg}$ $\Delta T_{3.9\_11} > \Delta T_{3.9\_11bg} + n_2 \times \delta T_{3.9\_11bg}$	$T_{3.8} - T_{3.8bg} > T_{TH1}$ $T_{3.8\_11} - T_{3.8\_11bg} > T_{TH2}$ $T_{THi} = \text{fun}(n_i, \theta s, P_v, P_c)$

Due to the large number of sun angles and rapid changes, the fire monitoring algorithm of the GK-2A satellite is more complicated than that of the polar orbiting satellite. It needs continuous improvement. When the zenith angle of the sun is close to 90 in the morning and evening hours, there is still a big problem in the reflectivity correction, and there is still a lot of room for improvement in the accuracy of fire point identification. The current threshold function was tested on samples from China and surrounding areas, so it has limitations in applicable areas. The threshold function for other regions needs to be studied further. Due to the low spatial resolution of GK-2A, it is difficult to obtain the underlying surface information in real time and accurately, which affects the identification results.

3.2. Fire Point Monitoring Algorithm Accuracy of Himawari-8 and GK-2A

In April 2021, different algorithms of Himawari-8 and GK-2A were used to monitor 1011 hot spots in the study area, respectively. Compared with the ground truth fire data, Compared with the original fire monitoring algorithm of Himawari-8, the present algorithm discrimination accuracy of GK-2A is increased by 8.4%, the average accuracy is increased by 9.1%, and the accuracy is increased by more than 9% (Table 4). From the perspective of time, 47% of the hot spots monitored by GK-2A are earlier than Himawari-8, and the sensitivity of fire point monitoring has been greatly improved. (Table 5).

Table 4. Fire monitoring algorithm effect for different satellites.

Satellite	Province	Total	Unconfirmed	Confirm	Discrimination Accuracy (%)	Average Precision (%)
Himawari-8	Guangdong	142	32	110	77.5	77.3
	Guangxi	303	64	239	78.9	
	Yunnan	444	97	347	78.2	
	Guizhou	91	29	62	68.1	
	Hainan	31	8	23	74.2	
GK-2A	Guangdong	142	19	123	86.5	86.4
	Guangxi	303	38	265	87.3	
	Yunnan	444	58	386	86.9	
	Guizhou	91	17	74	80.9	
	Hainan	31	5	26	84.5	

Table 5. Fire monitoring algorithm effect for different satellites.

	Percent (%)	$T_{3.8}$ (K)	$\Delta T_{3.8}$ (K)	T_{11} (K)	ΔT_{11} (K)
Early	47.1	294.3	6.72	287.4	0.27
Same	33.2	299.7	8.12	291.2	0.44
Delay	19.7	296.8	7.57	286.7	0.11

Compared with Himawari-8, the new algorithm of GK-2A has a good performance in fire point monitoring, but about 20% of the fire point has a lag phenomenon compared with Himawari-8. The accuracy and the timeliness of monitoring will be improved based on the joint fire point monitoring of the above two satellites.

3.3. Application

At 3:00 p.m. on 30 March 2020, a forest fire broke out in Xichang City, Liangshan Yi of the Autonomous Prefecture, Sichuan Province, and the fire spread rapidly towards Lushan Mountain. By 4:00 p.m. on 31 March, the burned area exceeded 1000 hm^2, and the destroyed area was more than 80 hm^2. By 2 April 2020, all open fires were extinguished. The Xichang forest fire was monitored and analyzed dynamically from 3:40 p.m. to 6:00 p.m. on March 30 by using GK-2A data. The specific steps are as follows. Firstly, the fire spot identification method of the human-computer interaction is used to identify fire spots from the 15-time subsatellite images from 3:40 p.m.–6:00 p.m. Figure 6 presents the original mid-infrared images from the GK-2A, with high brightness temperature in white and low brightness temperature in black. No obvious bright spot can be found in the infrared cloud image at 3:40 p.m., and a faint bright spot (red arrow) was visible in the infrared cloud image at 3:50 p.m. The fire spot was maintained faintly from 4:00 p.m. to 4:40 p.m., i.e., there was no noticeable change in the fire spot intensity during this period. From 4:50 p.m., the bright spot changed from a single point to a multi-point surface, with significantly increased brightness. This situation was maintained until 6:00 p.m. That is, the fire area started to expand outward during 4:50 p.m.–6:00 pm, and fire intensity increased significantly.

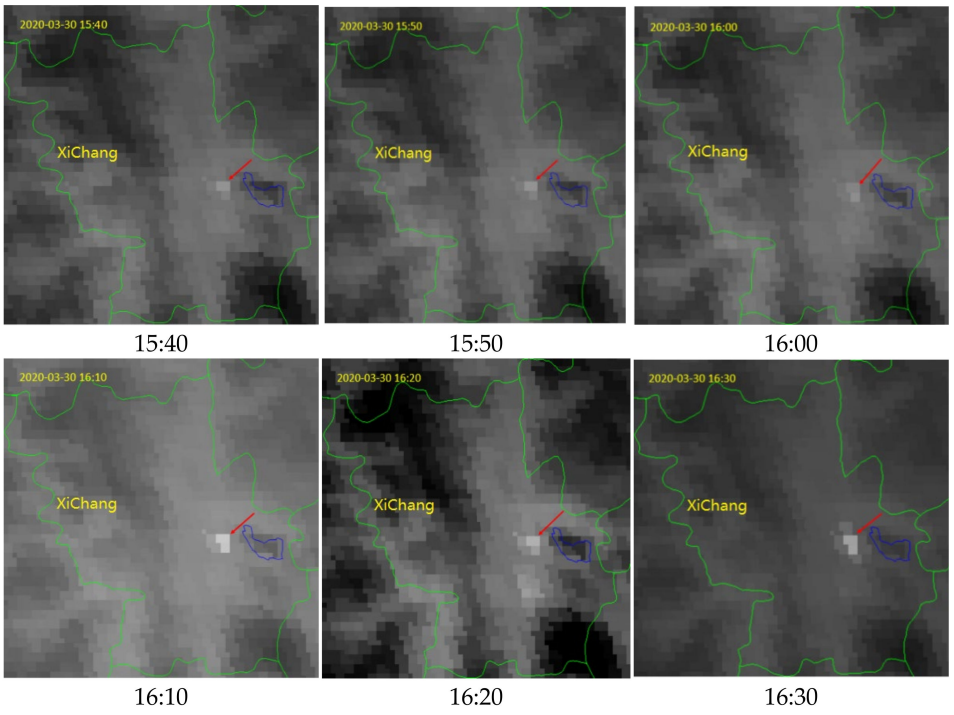

Figure 6. *Cont.*

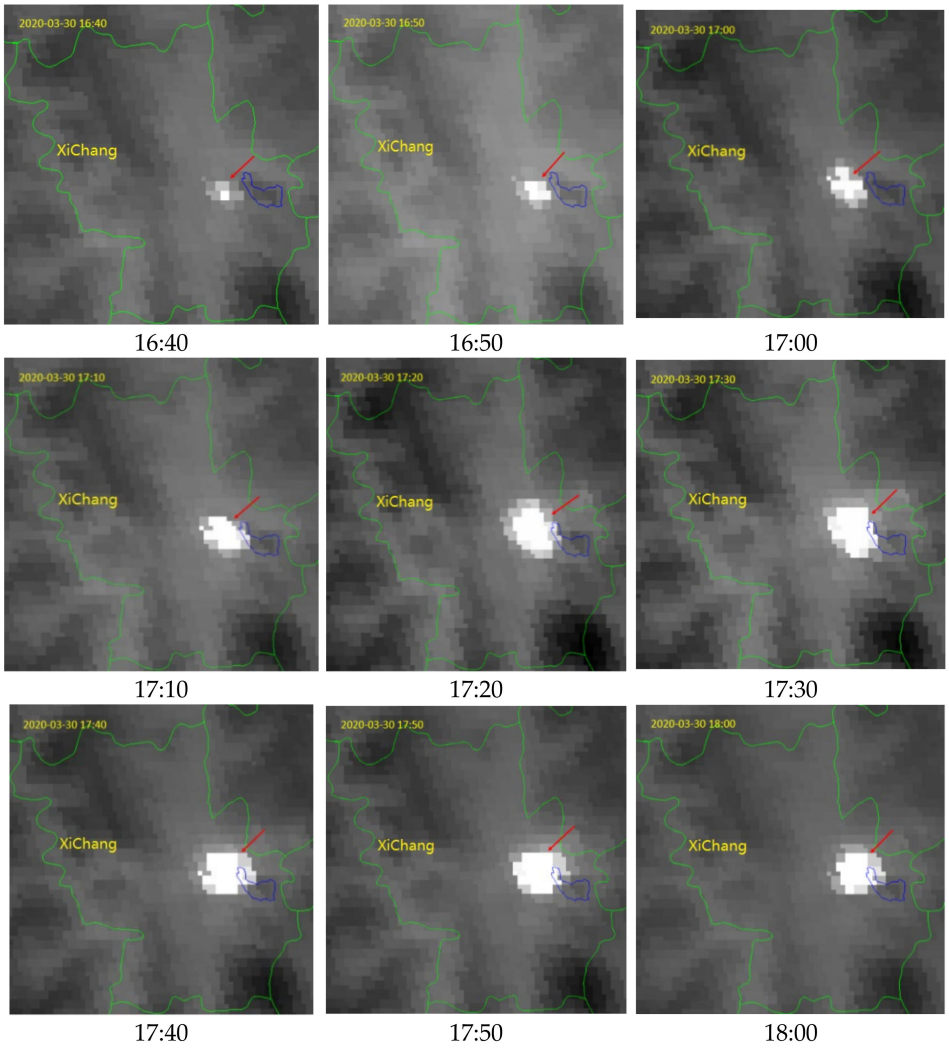

Figure 6. GK-2A mid-infrared images of forest fire detection in Xichang from 3:40 p.m. to 6:00 p.m. on 30 March 2020.

The physical parameters of satellite monitoring from 3:40 p.m. to 6:00 p.m. on 30 March (Table 6) suggest that at 3:40 p.m., the brightness temperature of the fire spot pixels was 310.2 K, and the background brightness temperature was 307.9 K. In addition, the brightness temperature differences between the fire spot pixels and background pixel did not reach the threshold value at that moment. Thus, neither algorithm identified the fire spot pixels.

From 3:50 p.m. to 6:00 p.m. (Table 6), the brightness temperature of the fire spot pixels increased from 314.5 K to 401 K. From 4:10 p.m., the brightness temperature at fire spot pixels increased more, and the difficulty of identifying the heat source pixels decreased in terms of both algorithms. The analysis of the situation at 3:50 p.m. and 4:00 p.m. reveals that the difference between the two algorithms lies in the change of the correction coefficients of background brightness temperature, and the correction coefficient of the original algorithm is larger than that of the new algorithm by 0.55 K (0.6 times). Thus, a higher brightness temperature difference is required for fire spot identification in the original algorithm than in the new one. Figure 6 demonstrates that the brightness temperature differences of pixels are not obvious. The main reason is that the fire spots were located around Xichang City, and the underlying surface type includes artificial buildings such as roads and houses, whose temperature increase rate is faster than that of forests. The introduction of correction information such as solar angle and forest coverage ratio parameters can effectively eliminate the impact of such interference on the background pixels of fire spots, improving the sensitivity and accuracy of fire spot identification.

A comprehensive analysis of the Xichang fire is conducted based on the GK-2A data at 10-min intervals for a total of 385 times from 3:40 p.m. on 30 March to 9:00 a.m. on 2 April 2020. Figure 7a shows the observation time of fire spots, Figure 7b presents the durations of fire spots, and Figure 7c indicates the variation of fire impact range with time.

As shown in Figure 7a, the main fire area can be obtained by the detection on 30 March, which spreads to the southeast. The burned area was mainly maintained within the main fire area on 31 March, 1 April and 2 April. Figure 7b shows that the maximum duration was more than 60 h, indicating that this fire has a large influence area and a long burning duration. Moreover, from Figure 7c, it can be found that the fire intensity has a cyclic variation, with five peaks on the afternoon of 30 March, the early morning, evening and night of 31 March and the night of 1 April, and a maximum instantaneous influence area of more than 20 hm^2. The periods of low fire intensity were mainly in the morning. Overall, the GK-2A satellite can monitor the positioning and fire intensity of fire spots at each time. Also, the GK-2A satellite data can be used to analyze the impact range and duration of the fire through the high-frequency observation of the minute interval of the satellite in order to obtain the highest risk area of the fire. The evolution of high-frequency fire intensity with time enables us to extract different high and low-risk periods and provide real-time and fine decision-making information for firefighters.

Table 6. Monitoring parameters of the "3.30" forest fire in Xichang.

Time	Solar Zenith Angle	Pixel Temperature (K)	The Temperature of Background (K)		Correction Coefficient		Fire (Yes/No)	
			New	Original	New	Original	New	Original
15:40	41.71	310.2	307.9	308.1	4.1	4.3	×	×
15:50	**43.72**	**314.5**	**307.8**	**308.2**	**4.2**	**4.7**	√	×
16:00	**45.71**	**315.4**	**307.9**	**308.6**	**5.1**	**5.8**	√	×
16:10	47.74	323.4	309.2	310.4	5.2	5.8	√	√
16:20	49.70	322.7	309.4	310.5	5.1	6.0	√	√
16:30	51.88	335.4	311.4	313.7	5.6	6.9	√	√
16:40	53.98	341.8	313.3	315.2	5.9	6.8	√	√
16:50	56.10	355.9	312.2	314.8	6.0	7.2	√	√
17:00	58.24	383.4	314.7	316.9	6.3	7.6	√	√
17:10	60.39	387.4	312.8	315.6	6.4	7.8	√	√
17:20	62.55	392.2	316.2	320.1	6.5	7.7	√	√
17:30	64.72	394.6	313.7	316.8	6.5	7.8	√	√
17:40	66.90	401	314.8	317.5	6.6	7.9	√	√
17:50	69.09	400.1	315.1	318.4	6.6	7.9	√	√
18:00	71.28	397.9	318.5	322.1	6.5	7.8	√	√

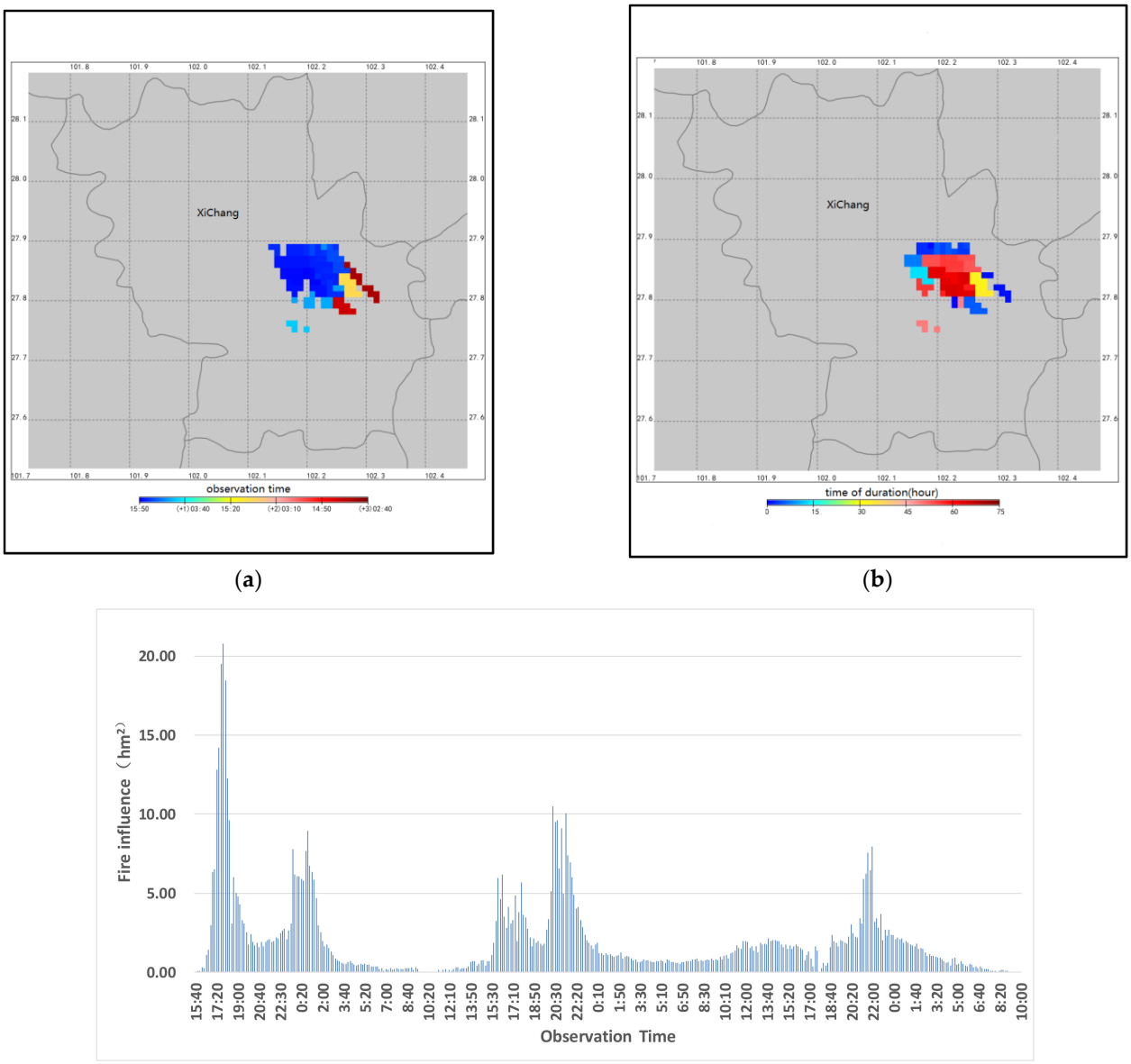

(**a**) (**b**)

(**c**)

Figure 7. Dynamic monitoring of the "3.30" forest fire in Xichang, Sichuan Province by the GK-2A satellite. (**a**) the observation time of fire spots, (**b**) the durations of fire spots, (**c**) the variation of fire impact range with time.

4. Conclusions

The data from the GK-2A satellite, the most advanced geostationary meteorological satellite, can be effectively applied to forest fire detection. This data can help us quickly and accurately obtain fire information such as fire spot location, area and temperature, and it plays an essential role in fire detection.

The fire spot identification algorithm of the GK-2A satellite is more scientific and reasonable than that of the Himawari-8 satellite. In this new algorithm, a new reflectivity correction method for solar angle is adopted during the data preprocessing, effectively ensuring the authenticity of the reflectivity information obtained at the large solar zenith angle. The proportional correction coefficient of the underlying surface type is introduced into the fire spot identification algorithm, which can effectively improve the accuracy and sensitivity of fire spot monitoring, especially for the complex underlying surface and the initial stage of fires.

The dynamic threshold problem of the fire point under the observation of the full sun elevation angle of the geostationary meteorological satellite is solved based on the GK-2A fire point monitoring algorithm in this study. This method considers different sun angle, cloud cover and vegetation coverage conditions based on the algorithms of MODIS and Himawari-8. It improves the misjudgment caused by the sun reflection at the edge of the cloud and the underlying surface of sparse vegetation. The accuracy of the present fire point monitoring algorithm v of GK-2A is more than 9% higher than the original Himawari-8 fire monitoring.

Moreover, due to the high timeliness of remote sensing technology, the GK-2A satellite can perform high-frequency and timely observation during fire detection. The multi-time and continuous observation can be used to evaluate the influence range and intensity of fires in real time and obtain continuous and dynamic fire information, which is of great significance for the real-time observation, fire development and rapid assessment of forest fires. The detection of the 3.30 Xichang forest fire in 2020 further demonstrates the critical role of the GK-2A satellite data in forest fire detection, which can provide a basis for the forest and grassland fire prevention departments to take fire prevention measures in time.

Author Contributions: Data curation, J.C. and W.Z.; Funding acquisition, W.Z. and J.C.; Investigation, J.C., W.Z., C.L. and H.Y.; Methodology, J.C., W.Z., S.W., C.L. and H.Y.; Project administration, J.C., W.Z. and S.W.; Writing—original draft, J.C.; Writing—review & editing, S.W. All authors have read and agreed to the published version of the manuscript.

Funding: This research was funded by National Key R&D Program of China [Grant Number 2021YFC3000300].

Conflicts of Interest: The authors declare no conflict of interest.

References

1. Lu, A.; Tian, H.; Liu, Y. State-of-the-Art in quantifying fire disturbance and ecosystem carbon cycle. *Acta Ecol. Sinca* **2005**, *25*, 2734–2743.
2. Abram, N.J.; Henley, B.J.; Sen Gupta, A.; Lippmann, T.J.R.; Clarke, H.; Dowdy, A.J.; Sharples, J.J.; Nolan, R.H.; Zhang, T.R.; Wooster, M.J.; et al. Connections of climate change and variability to large and extreme forest fires in southeast Australia. *Commun. Earth Environ.* **2021**, *2*, 8. [CrossRef]
3. Brandes, A.F.D.; Sanchez-Tapia, A.; Sansevero, J.B.B.; Albuquerque, R.P.; Barros, C.F. Fire records in tree rings of Moquiniastrum polymorphum: Potential for reconstructing fire history in the Brazilian Atlantic Forest. *Acta Bot. Bras.* **2019**, *33*, 61–66. [CrossRef]
4. White, B.L.A. Spatiotemporal variation in fire occurrence in the state of Amazonas, Brazil, between 2003 and 2016. *Acta Amazonica* **2018**, *48*, 358–367. [CrossRef]
5. Soro, T.D.; Koné, M.; N'Dri, A.B.; Touré, N.E. Identified main fire hotspots and seasons in Cote d'Ivoire (West Africa) using MODIS fire data. *S. Afr. J. Sci.* **2021**, *117*, 1–13. [CrossRef]
6. Giglio, L.; Csiszar, I.; Justice, C.O. Global distribution and seasonality of active fires as observed with the Terra and Aqua Moderate Resolution Imaging Spectroradiometer (MODIS) sensors. *J. Geophys. Res. Biogeosci.* **2006**, *111*, G02016. [CrossRef]
7. Le Page, Y.; Oom, D.; Silva, J.M.N.; Jonsson, P.; Pereira, J.M.C. Seasonality of vegetation fires as modified by human action: Observing the deviation from eco-climatic fire regimes. *Glob. Ecol. Biogeogr.* **2010**, *19*, 575–588. [CrossRef]
8. Fusco, E.J.; Finn, J.T.; Abatzoglou, J.T.; Balch, J.K.; Dadashi, S.; Bradley, B.A. Detection rates and biases of fire observations from MODIS and agency reports in the conterminous United States. *Remote Sens. Environ.* **2019**, *220*, 30–40. [CrossRef]
9. Lin, Z.Y.; Chen, F.; Li, B.; Yu, B.; Shirazi, Z.; Wu, Q.C.; Wu, W. FengYun-3C VIRR Active Fire Monitoring: Algorithm Description and Initial Assessment Using MODIS and Landsat Data. *IEEE Trans. Geosci. Remote Sens.* **2017**, *55*, 6420–6430. [CrossRef]
10. Shan, T.C.; Zheng, W.; Chen, J.; Tang, S.H. A burned area mapping method for the FY-3D MERSI based on the single-temporal L1 data and multi-temporal daily active fire products. *Int. J. Remote Sens.* **2021**, *42*, 1292–1310. [CrossRef]
11. Zhang, J.H.; Yao, F.M.; Liu, C.; Yang, L.M.; Boken, V.K. Detection, Emission Estimation and Risk Prediction of Forest Fires in China Using Satellite Sensors and Simulation Models in the Past Three Decades—An Overview. *Int. J. Environ. Res. Public Health* **2011**, *8*, 3156–3178. [CrossRef] [PubMed]
12. Eskandari, S.; Ghadikolaei, J.O.; Jalilvand, H.; Saradjian, M.R. Evaluation of the MODIS Fire-Detection Product in Neka-Zalemroud Fire-Prone Forests in Northern Iran. *Pol. J. Environ. Stud.* **2015**, *24*, 2305–2308.
13. Chuvieco, E.; Lizundia-Loiola, J.; Pettinari, M.L.; Ramo, R.; Padilla, M.; Tansey, K.; Mouillot, F.; Laurent, P.; Storm, T.; Heil, A.; et al. Generation and analysis of a new global burned area product based on MODIS 250 m reflectance bands and thermal anomalies. *Earth Syst. Sci. Data* **2018**, *10*, 2015–2031. [CrossRef]

14. Giglio, L.; Schroeder, W.; Justice, C.O. The collection 6 MODIS active fire detection algorithm and fire products. *Remote Sens. Environ.* **2016**, *178*, 31–41. [CrossRef]
15. Boschetti, L.; Roy, D.P.; Justice, C.O.; Humber, M.L. MODIS-Landsat fusion for large area 30 m burned area mapping. *Remote Sens. Environ.* **2015**, *161*, 27–42. [CrossRef]
16. Gong, A.D.; Li, J.; Chen, Y.L. A Spatio-Temporal Brightness Temperature Prediction Method for Forest Fire Detection with MODIS Data: A Case Study in San Diego. *Remote Sens.* **2021**, *13*, 2900. [CrossRef]
17. Bessho, K.; Date, K.; Hayashi, M.; Ikeda, A.; Imai, T.; Inoue, H.; Kumagai, Y.; Miyakawa, T.; Murata, H.; Ohno, T.; et al. An Introduction to Himawari-8/9-Japan's New-Generation Geostationary Meteorological Satellites. *J. Meteorol. Soc. Japan* **2016**, *94*, 151–183. [CrossRef]
18. Liu, X.; He, B.; Quan, X.; Yebra, M.; Qiu, S.; Yin, C.; Liao, Z.; Zhang, H. Near Real-Time Extracting Wildfire Spread Rate from Himawari-8 Satellite Data. *Remote Sens.* **2018**, *10*, 1654. [CrossRef]
19. Giglio, L.; Descloitres, J.; Justice, C.O.; Kaufman, Y.J. An Enhanced Contextual Fire Detection Algorithm for MODIS. *Remote Sens. Environ.* **2003**, *87*, 273–282. [CrossRef]
20. Kaufman, Y.J.; Justice, C.O.; Flynn, L.P.; Kendall, J.D.; Prins, E.M.; Giglio, L.; Ward, D.E.; Menzel, W.P.; Setzer, A.W. Potential global fire monitoring from EOS-MODIS. *J. Geophys. Res.* **1998**, *103*, 32215–32238. [CrossRef]
21. Xu, G.; Zhong, X. Real time wildfire detection and tracking in Australia using geostationary satellite:Himawari 8. *Remote Sens. Lett.* **2017**, *8*, 1052–1061. [CrossRef]
22. Wickramasinghe, C.; Wallace, L.; Reinke, K.; Jones, S. Intercomparison of Himawari-8 AHI-FSA with MODIS and VIIRS active fire products. *Int. J. Digit. Earth* **2020**, *13*, 457–473. [CrossRef]
23. Chang, K.K.; Kim, H.G.; Kang, Y.H.; Yun, C.Y.; Lee, Y.G. Intercomparison of Satellite-Derived Solar Irradiance from the GEO-KOMSAT-2A and HIMAWARI-8/9 Satellites by the Evaluation with Ground Observations. *Remote Sens.* **2020**, *12*, 2149.
24. Chen, J.; Zheng, W.; Liu, C. Application of grassland fire monitoring based on Himawari-8 geostationary meteorological satellite data. *J. Nat. Disasters* **2017**, *26*, 197–204.
25. Zhou, Y.; Sui, S.; Chen, J.; Zhou, E.; Huang, Y.; Wang, T. Monitoring and Alarm Technology of Wildfire Occurrences in Transmission Lines Corridors Based on Himawari-8 Geostationary Meteorological Satellite. *High Volt. Eng.* **2020**, *46*, 2561–2569.
26. Zhao, W.; Shan, H.; Zhang, Y. Approach to the fire detection technology and the algorithm from the geostationary Himawari-8. *J. Saf. Environ.* **2019**, *19*, 2063–2073.
27. Lee, K.S.; Chung, S.R.; Lee, C.; Seo, M.; Choi, S.; Seong, N.H.; Jin, D.; Kang, M.; Yeom, J.M.; Roujean, J.L.; et al. Development of Land Surface Albedo Algorithm for the GK-2A/AMI Instrument. *Remote Sens.* **2020**, *12*, 2500. [CrossRef]
28. Oh, S.M.; Borde, R.; Carranza, M.; Shin, I.C. Development and Intercomparison Study of an Atmospheric Motion Vector Retrieval Algorithm for GEO-KOMPSAT-2A. *Remote Sens.* **2019**, *11*, 2054. [CrossRef]
29. Wang, J.; Liu, C.; Yang, L.; Shang, J.; Zhang, Z. Calculation of Geostationary Satellites′ Nominal Fixed Grid and Its Application in FY-4A Advanced Geosynchronous Radiation Imager. *Acta Optica Sinica* **2018**, *38*, 1211001-1–1211001-9. [CrossRef]
30. Goncalves, H.; Goncalves, J.A.; Corte-Real, L. Measures for an Objective Evaluation of the Geometric Correction Process Quality. *IEEE Geosci. Remote Sens. Letters* **2009**, *6*, 292–296. [CrossRef]
31. Di Biase, V.; Laneve, G. Geostationary sensor based forest fire detection and monitoring: An improved version of the SFIDE algorithm. *Remote Sens.* **2018**, *10*, 741. [CrossRef]
32. Filizzola, C.; Corrado, R.; Marchese, F.; Mazzeo, G.; Paciello, R.; Pergola, N.; Tramutoli, V. RST-FIRES, an exportable algorithm for early-fire detection and monitoring: Description, implementation, and field validation in the case of the MSG-SEVIRI sensor. *Remote Sens. Environ.* **2016**, *186*, 196–216. [CrossRef]
33. Schroeder, W.; Oliva, P.; Giglio, L.; Csiszar, I.A. The new VIIRS 375 m active fire detection data product: Algorithm description and initial assessment. *Remote Sens. Environ.* **2014**, *143*, 85–96. [CrossRef]
34. Na, L.; Zhang, J.; Bao, Y.; Bao, Y.; Na, R.; Tong, S.; Si, A. Himawari-8 satellite based dynamic monitoring of grassland fire in China-Mongolia border regions. *Sensors* **2018**, *18*, 276. [CrossRef]
35. Jang, E.; Kang, Y.; Im, J.; Lee, D.W.; Yoon, J.; Kim, S.K. Detection and Monitoring of Forest Fires Using Himawari-8 Geostationary Satellite Data in South Korea. *Remote Sens.* **2019**, *11*, 271. [CrossRef]